ACS APPLIED MATERIALS & INTERFACES

Research Article

www.acsami.org

Synthesis on Winged Graphene Nanofibers and Their Electrochemical Capacitive Performance

Chengshi Gong,[†] Yongmin He,[†] Jinyuan Zhou,[†] Wanjun Chen,[†] Weihua Han,*[,†] Zhenxing Zhang,[†] Peng Zhang,[†] Xiaojun Pan,[†] Zhiguang Wang,[‡] and Erqing Xie*[,†]

[†]School of Physical Science and Technology, Lanzhou University, Lanzhou 730000, China

[‡]Institute of Modern Physics, Chinese Academy of Sciences, Lanzhou 730000, China

Supporting Information

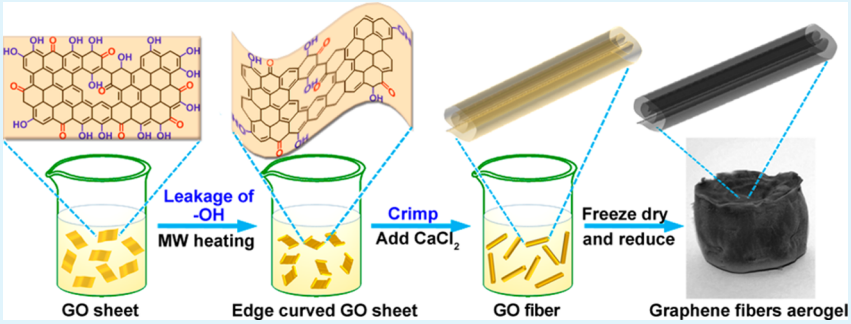

ABSTRACT: Assembly techniques of graphene have attracted intense attention since their performance strongly depends on the manners in which graphene nanosheets are arranged. In this work, we demonstrate a viable process to synthesize winged graphene nanofibers (G-NFs) which could generate optimized pore size distribution by the fiber-like feature of graphene. The G-NF frameworks were achieved by processing the precursor graphene oxide nanosheets with the following procedures: microwave (MW) irradiation, salt addition, freeze-drying, and chemical reduction. The resultant framework composed of winged G-NFs with a diameter of 200−500 nm and a length of 5−20 μm. Moreover, the crimp degree of G-NFs can be rationally controlled by MW irradiation time. A formation mechanism of such winged G-NFs based on the synergistic effects from MW irradiation and solution ionic strength change has been proposed. With a practice in flexible electrode, after decorated with amorphous MnO_2, the G-NF frameworks shows an enhanced specific capacitance compared to graphene nanosheets (G-NSs). This research has developed a controllable method to synthesis G-NFs, which can offer hierarchical pore structures, this kind of graphene nanostructure might enhance their performance in supercapacitor and related fields.

KEYWORDS: *graphene nanofiber, three-dimensional framework, microwave irradiation, ionic strength, capacitive performance*

1. INTRODUCTION

Since its discovery in 2004, graphene, as a typical two-dimensional (2D) colloid made up of only several atomic layers of sp^2-hybridized carbon atoms in a honeycomb lattice, has attracted persistent attention.[1] And graphene-based materials have been successfully applied into transistors,[2,3] sensors, and optoelectronics[4] because of their superior electrical, mechanical and optical properties.[5,6] Nowadays, the integration technique of graphene nanosheets (G-NSs) into macroscopic structures is attracting more and more interests, since it is an essential step in exploring the unique properties of individual 2D nanosheets for practical applications.[7] So far, using bottom-up self-assembly or template-assembly methods, many macroscopic architectures made up of G-NSs have been obtained, such as spheres,[8,9] fibers/tubes,[10,11] papers/films,[12,13] and three-dimensional (3D) frameworks.[14−16]

Among these architectures, 3D graphene architectures have become one of the hotspot in the material field due to their well-defined and cross-linked 3D porous structure as well as high specific surface area, which make them commonly used as electrodes of electrochemical capacitors (ECs).[17] Furthermore, to improve the porosity of 3D graphene architectures, researchers usually introduce carbon nanofibers and nanotubes into 3D graphene frameworks and obtained higher EC performances as previously reported.[15,16,18] However, accompanying with the excellent properties of the assemblies, the complicated synthesize procedure of carbon nanotube/nanofibers on 3D graphene backbone and strict conditions have to be involved into assembling the composited structure. To address the problem, it is urgent to develop an effective method to assemble the alternative G-NSs into graphene nanofiber (G-NF)-based 3D frameworks in a controllable, uniform and a large-scale manner for practical applications. It suggests that the graphene-based nanofibers should possess high porosity and

Received: March 17, 2014
Accepted: August 8, 2014
Published: August 8, 2014

nanoscale dimension, which can result in better EC performance than traditional neat carbon fibers.[19,20]

In comparison, macroscopic neat graphene fibers have been well-assembled with wet spinning high concentrated liquid crystalline graphene oxide,[11,21] or by a complex template strategy,[22] and using a self-assembling procedure.[23] However, most of these fibers are assembled by abundant 2D graphene nanosheets with strong $\pi-\pi$ interaction between each other. As a result, the assembling method leads to the stacked graphene fibers with thick diameter (several micrometers) and smooth surface as well as low specific surface area,[10] which would limit its application in energy storage systems. Though many efforts have been spent on the synthesis of graphene-based fibers, it remains a great challenge to assemble one or several 2D graphene oxide nanosheets (GO-NSs) into carbon nanofiber and nanoscroll-like structures,[24,25] mainly because of the asymmetric sizes, irregular shapes, strong restacking tendency of G-NSs, as well as the lack of the effective assembly technique. The unclear formation mechanism of the G-NFs is another issue that hinder their further development.[26] Therefore, it is important to develop a versatile and controllable method to synthesize 3D macroscopic G-NF frameworks for their potential application in electrochemical energy storage systems.

In this work, we report a simple and controllable method to synthesis 3D macroscopic G-NF frameworks. We directly assemble 2D GO-NSs into graphene oxide nanofibers (GO-NFs) in a solution environment under the synergistic effects from microwave (MW) irradiation and the change of solution ionic strength. In this case, we proposed an electrostatic force induced crimping mechanism for the formation of the G-NFs. Furthermore, as expected, flexible electrodes constructed from the obtained G-NF frameworks show enhanced electrochemical performances compared to those of 3D G-NSs. This research suggests a more design-rich strategy to build the G-NF-based 3D macroscopic graphene frameworks using 2D graphene nanosheets.

2. EXPERIMENTAL SECTION

2.1. Preparation of GO-NSs and G-NSs. GO-NSs were synthesized using high-purity graphite powder via a modified Hummer's method.[27] In a typical fabrication process, 10 mL of GO suspension (0.5 mg/mL) was first fed into a 25 mL beaker, the baker was then dipped in liquid nitrogen in order to quickly freeze the suspension into ice. The frozen suspension was then put into a high vacuum chamber and processing vacuum drying 24 h to thoroughly remove the residual water in the suspension (final vacuum of 1.0×10^{-4} Pa was achieved). The GO aerogel can be obtained after these procedures. The G-NS frameworks were obtained by reducing the as-prepared GO-NS frameworks with hydroiodic acid (HI) for 1 h at 95 °C. Finally, to improve the mechanical performance, the obtained G-NSs aerogel was cut into rectangular strips and pressed under an optimal pressure (~1 MPa) to form a flexible film (Figure 1c) with a thickness of ~100 μm and areal density of ~1.5 mg/cm^2.

2.2. Formation of GO- and G-NF Frameworks. The GO fibers were typically synthesized with the following procedures: first, 10 mL of GO suspension (0.5 mg/mL) was feed into an 80 mL sealed glass bottle and irradiated for 0–9 min at 700 W with a microwave oven (Galanz, G70D20P-TD, China). After the suspension naturally cooled to room temperature, 200 μL of $CaCl_2$ solution (10 mg/mL) was injected into the MW treated GO suspension, followed by a 10 min stirring procedure. Subsequently, the cold mixture was transferred into a 25 mL beaker for 24 h of freeze-drying, and the GO-NF frameworks were achieved. Finally, the G-NFs were obtained by reducing the as-prepared GO-NFs with HI for 1 h at 95 °C. The flexible G-NFs film was also prepared with a thickness of ~98 μm and area density of 1.6 mg/cm^2. In addition, to explore the formation mechanism of GO-NFs, the influence of MW treating time, $CaCl_2$, and GO concentration were also investigated.

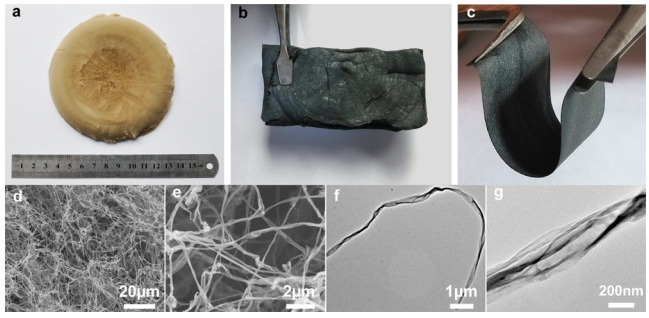

Figure 1. Photographs of (a) GO aerogel with a diameter of 10 cm prepared by freeze-drying the preprocessed GO solution, (b) reduced graphene aerogel and (c) the obtained flexible graphene film by a suitable pressure; (d) SEM image of graphene aerogel and (e) its magnified image; (f) TEM image of single G-NF and (g) corresponding HR-TEM image.

2.3. Deposition of MnO_2 Active Layers. The obtained G-NF frameworks were washed with ethanol and deionized water repeatedly. A piece of 1 cm × 1 cm clean G-NF frameworks were then infiltrated into an aqueous 0.1 M Na_2SO_4 solution and kept for 2 h. After that, the G-NF frameworks were soaked in a mixture of Na_2SO_4 (50 mL, 0.1 M) and $KMnO_4$ solution (50 mL, 0.1 M) for 1 h, and then washed with deionized water for several times to remove the adsorbed $KMnO_4$. Finally, the as-obtained MnO_2/G-NF composites were stored in a 1 M Na_2SO_4 solution and waiting for further EC measurements. For comparison, MnO_2/G-NS composites were also prepared with the same procedures.

2.4. Characterization Methods. The morphology of the obtained samples was characterized by field emission scanning electron microscope (FE-SEM, Hitachi S-4800, accelerating voltage of 5 kV). The fine microstructures were systematically studied using high-revolution transmission electron microscope (HR-TEM, FEI Tecnai F30, operated at 300 kV). X-ray diffraction (XRD, Philips, X'pert pro, CuKα, 0.154056 nm), and micro-Raman spectroscope (JY-HR800, YAG laser, 532 nm, spot diameter ~600 nm) were used to analysis the phase and component. The chemical elements and bonds were analyzed on a PHI-5702 multifunctional X-ray photoelectron spectroscope (XPS) using Mg Kα X-ray ($h\nu$ = 1253.6 eV) as the excitation source. The mass of the MnO_2 deposited on the frameworks was measured by a microbalance (Mettler, XS105DU). Electrochemical measurements were performed on an electrochemical workstation (RST5200, Zhengzhou Shiruisi, China) at ambient conditions.

3. RESULTS AND DISCUSSION

3.1. Morphology of Typical G-NFs Network. The GO-NFs framework was obtained using a type of GO aqueous suspension as material, which contains GO-NSs with an average diameter of 36 μm (see the Supporting Information, Figure S1), and the process consists of three steps: (i) treat the GO aqueous suspension with MW irradiation; (ii) change the ionic strength of the GO aqueous suspension with $CaCl_2$; (iii) freeze-dry the treated GO aqueous suspension to obtain 3D GO frameworks. As shown in Figure 1a, after freeze-drying, a brown GO aerogel with a diameter of about 10 cm was drawn out from the baker. Then, the as-prepared aerogel was reduced into graphene one using chemical reduction methods, as shown in Figure 1b. After reduction, the color of the aerogel changed from brown to black. Generally, the reduced aerogel has a loose structure, which lose weak mechanical properties and limit its application in a flexible supercapacitor. To improve their mechanical performance, the obtained graphene aerogels were pressed into flexible films (Figure 1c) under an optimal pressure (~1 MPa) for further

characterization. The microstructures of pressed G-NSs and G-NFs were shown in Figure S2 in the Supporting Information. Pressed G-NFs exhibits a porous structure and G-NSs shows a relatively compact structure. The interconnected pore structure of pressed G-NFs are mainly attributed to the fiber-like feature of graphene.

The morphologies of the graphene aerogels were investigated by SEM and TEM. Figure 1d is a typical SEM image of graphene aerogel. It can be seen that the 3D graphene aerogel is consisted of winged G-NFs, the length of G-NFs was obtained from several TEM images of detached G-NFs (like Figure 1f) and ranges from 5 to 20 μm. The diameter was obtained from high-magnification SEM and TEM images and varies from 200 to 500 nm (Figure 1e, g). A high-magnification SEM image (Figure 1e) indicates that the G-NFs interconnected together, and these fibers formed a highly porous 3D framework. Further TEM characterization shows that each winged G-NF is composed by one or several G-NSs (Figure 1f). In addition, HR-TEM image (Figure 1g) showed that these winged G-NFs have a rough and crumpled surface, which is different from the reported neat graphene fibers.[22,23] In addition, SEM images of GO fibers were also demonstrated in Figure S3 in the Supporting Information, the morphology of GO fibers is nearly the same as the G-NFs which indicates that the reduction procedure did not change the fiber-like structure of GO. The conductivity of G-NSs and G-NFs is 23 S/cm and 27 S/cm, respectively. The relatively higher conductivity of G-NFs may be attributed to the interconnected structure of graphene nanofibers, as shown in Figure 1e.

3.2. Morphology Tuned by MW and Salt. To explore the formation mechanism, we also investigated the effects of MW and salt on the structures of the GO aerogels.

3.2.1. Effect of MW Irradiation. MW was chosen as the induction source due to its selective heating effect generated by high resonance with hydroxyl groups.[28,29] Before MW irradiation, the pristine GO-NSs are sheetlike as shown in Figure 2a. A higher

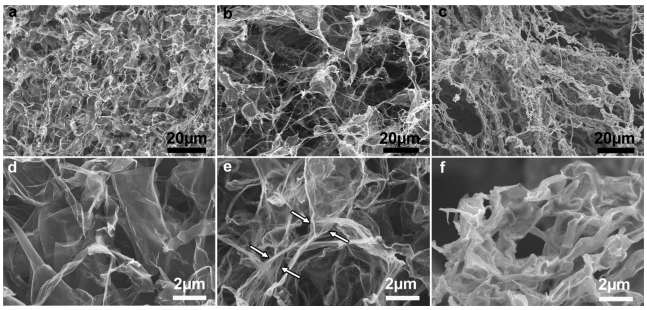

Figure 2. SEM images of (a) the pristine GO-NSs, (b) the edge curved GO-NSs obtained from the 3 min MW-irradiated GO solution, and (c) the GO clusters obtained from the GO solution added with $CaCl_2$, (d–f) corresponding higher-magnification SEM images of a–c.

magnification image shown in Figure 2d shows that the NSs are flat in the middle and slightly curling at the edge. After processing by MW, the GO-NSs began to wrinkle and strongly crimped at the edge, as shown in Figure 2b, e. The crimp degree of GO-NSs is highly dependent on the treating time of MW as illustrated in Figure S4 in the Supporting Information.

Furthermore, to explore why the flat GO-NSs can wrinkle into the edge curved GO-NSs under the MW irradiation, micro-Raman and XPS were used to investigate the change of chemical bonds in the samples during the MW irradiation. The Raman spectrum of pristine GO-NSs shows two characteristic bands at 1369 cm^{-1} (D band) and 1608 cm^{-1} (G band), respectively (Figure 3a). After MW irradiation for 9 min, the D and

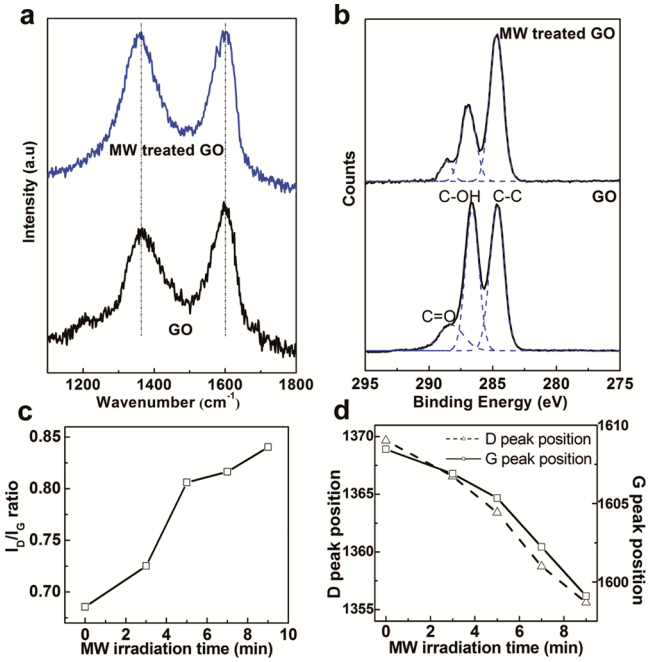

Figure 3. (a) Raman and (b) C 1s XPS spectra for of the pristine and MW-irradiated (9 min) GO-NSs, (c) I_D/I_G ratio change, (d) D and G peak position shift of GO-NSs as a function of MW irradiation time.

G bands shift to 1355 and 1599 cm^{-1}, as shown in Figure 3c. The blue shift of D and G bands are proportional to MW irradiating time, indicating the reduction of GO during microwave treatment.[30,31] The intensity ratio of D and G bands, i.e. I_D/I_G, gradually changes from 0.69 to 0.84 (Figure 3d) as increasing the MW irradiation time, which indicates an increase in the average size of sp^2 domain upon the deoxygenating of GO by microwave treatment.[32] The unexpected phenomena for the intensity increasing of D band is also found by other groups.[33,34] Stankovich et al.[32] suggested that reduction increases the number of aromatic domains of smaller overall size in graphene, which would lead to an increase of the I_D/I_G ratio.

XPS measurements could provide the direct evidence of the deoxygenation of GO during the microwave treatment. Figure 3b shows the XPS patterns of GO and the microwave treated GO (9 min). The C 1s XPS spectrum of pristine GO-NSs can be deconvoluted into three peaks at 284.6, 286.7, and 288.0 eV, which can be assigned to C–C, C–OH, and C═O bonds, respectively.[35] After irradiated by MW, the intensity of C–OH in the samples greatly decreases from 100% to 50%, while the intensity of C═O bonds decreases a little. At the same time, the C/O ratio changes from 2.52 to 3.39, indicating the selective dehydroxylation of GO as MW irradiation.

In addition, from the optical images of GO suspensions at different MW treating time (see Figure S5 in the Supporting Information), it can be more intuitively confirmed that the color of the GO suspension changes from brown to black due to their reduction reaction.[36] Moreover, it can also be seen that the volume of the obtained GO aerogel blocks decreases with the MW treating time after freeze-drying (see Figure S6 in the Supporting Information), indicating the stacking of the GO-NSs after long time MW irradiation.

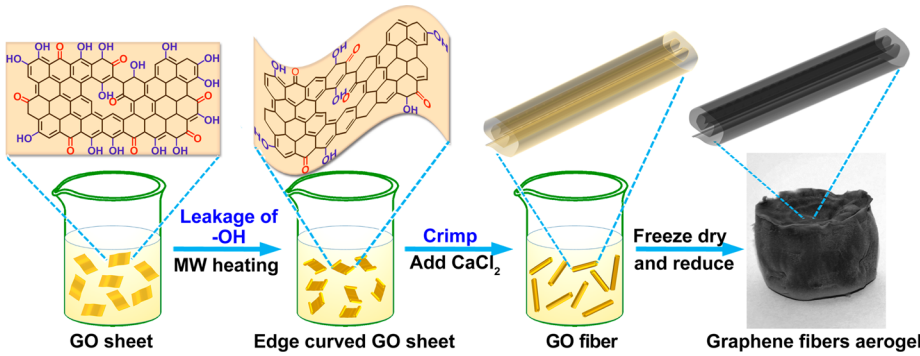

Figure 4. Schematic illustration of the crumpling mechanism of the graphene nanofiber.

3.2.2. Effect of Ionic Strength. On the other hand, the ionic strength of GO suspension can also influence the microstructures of the obtained GO aerogel. Figure 2c shows the SEM images of GO-NSs obtained from pristine GO solution by only adding with 3 mM $CaCl_2$ and no MW-irradiation treatments. It can be seen that the GO-NSs greatly aggregate into clusters under the strong ionic strength. Furthermore, from the high-magnification image (Figure 2f); it is found that the obtained GO-NSs present a densely stacked structure, which is rather different from that of the sheetlike structure of GO-NSs (Figure 2d). Therefore, it can be indicated that the ionic strength changing by adding $CaCl_2$ shows stronger curly ability than that of MW irradiation reduction. However, no matter how we change the ion concentration of GO suspension without MW irradiation, the GO-NSs could not form nanofibers structure, as shown in Figure S7 in the Supporting Information.

Therefore, we could suppose that the MW irradiation play a critical guiding role in the formation of the winged GO-NFs, and the ionic strength of GO suspension enhanced by salt addition will further improve the wrinkling rate of GO-NSs.

3.3. Formation Mechanism of Macroscopic GO Nanofibers. According to aforementioned investigations on chemical bonds in GO-NSs, an electrostatic force induced crimping formation mechanism for the formation of the winged GO-NFs is proposed, as schematically shown in Figure 4, as follows

(i) Most of GO-NSs synthesized through the modified Hummer's method can well dispersed in water due to abundant functional groups on its edges and basal planes (especially on the edge of GO-NSs). These groups make GO-NSs carry a negative charge and keep a flat morphology in water under strong in-planar electrostatic repulsion.[37]

(ii) When irradiated by the MW, the polar molecules such as hydroxyl (−OH) groups will selectively fall into a high resonance.[38−40] As a result, the −OH groups absorbed on the edge of GO-NSs will quickly escape as described by the following equation

$$C_6O_x{-}(OH)_y \xrightarrow{\text{MW irradiation}} C_6O_x{-}(OH)_{y-b} + b(-OH) \quad (1)$$

in which x and y (≤ 6) are the number of =O and −OH groups in carbon hexahydric rings of the GO-NSs, respectively. The dehydroxylation process is similar to the typical chemical reduction process by alkaline.[41] As part of the hydroxyl groups on the GO-NSs are removed, the flat GO-NSs will crimp first from the edge because of the unbalance of the electrostatic state of GO-NSs.[37]

(iii) Generally, once $CaCl_2$ is added into the pristine GO suspension, GO-NSs will quickly stack under strong ionic strength because of the surface charge of GO destabilized by addition of salt.[37,42] However, when GO-NS was first irradiated by MW, the $CaCl_2$ addition will prompt the formation of GO-NFs instead of stacking into clusters of GO-NSs. Here, it can be stated that after the MW irradiation, the GO-NSs will initially crimp under the unbalance of the electrostatic state between GO-NSs. Once the $CaCl_2$ was added, the unbalance of the electrostatic state would increase, which enhances the crimping of the NSs and form winged GO-NFs. Furthermore, the crimping degree of GO-NFs is strictly controlled by MW treating time, as shown in Figure S8 in the Supporting Information.

Subsequently, freeze-drying process was used to prepare GO-NF frameworks. Further control experiments (see Figure S9 in the Supporting Information) indicate that freeze-drying process can help to avoid the deformation of GO-NFs and obtain 3D frameworks. Finally, a HI chemical reduction was employed to obtain black G-NF frameworks. On the other hand, the GO concentration will determine the final morphology of the graphene (fiber-like or sheet-like). It can be seen that the amount of fibers decreases when the GO concentration increases from 0.5 to 2 mg/mL, and no visible fiber-like GO formed at high concentration (see Figure S10 in the Supporting Information). For GO solution at high concentration, the limited space between two adjacent GO sheets (as shown in Figure S10c in the Supporting Information) hinders the crumpling process of GO nanosheets which leads to the formation of 3D GO sheets structure.

3.4. EC Measurements. Before EC measurements, MnO_2 was chosen as an active material and loaded on the obtained graphene networks to improve their capacitive performances. To obtain MnO_2/G-NF composites, we dipped the G-NFs frameworks into a solution of 0.1 M $KMnO_4$/0.1 M Na_2SO_4 at neutral PH value for 1 h. During this procedure, MnO_2 can be uniformly coated onto the 3D porous structures based on self-limiting deposition.[43] After the deposition of MnO_2, the obtained 3D macroporous MnO_2/G-NF composites were investigated by scanning TEM (STEM). Figure 5a is the typical high-angle annular dark-field STEM (HAADF-STEM) of the MnO_2/G-NF composites. As shown in the high-resolution HADDF image (Figure 5f), flocculent-like MnO_2 were uniformly coated on G-NF backbones and fiberlike feature of G-NFs was not affected by the MnO_2 deposition (Figure 5a). Figure 5b is an energy-dispersive X-ray spectroscopic (EDX) spectrum of the obtained MnO_2/G-NF composites, which indicates that the fibers are mainly made up of C, Mn, and O. The Cu elements are attributed to the TEM grids used in the measurements. EDX elemental mapping images of C, O, and Mn within the area marked with a red square frame in Figure 5a,

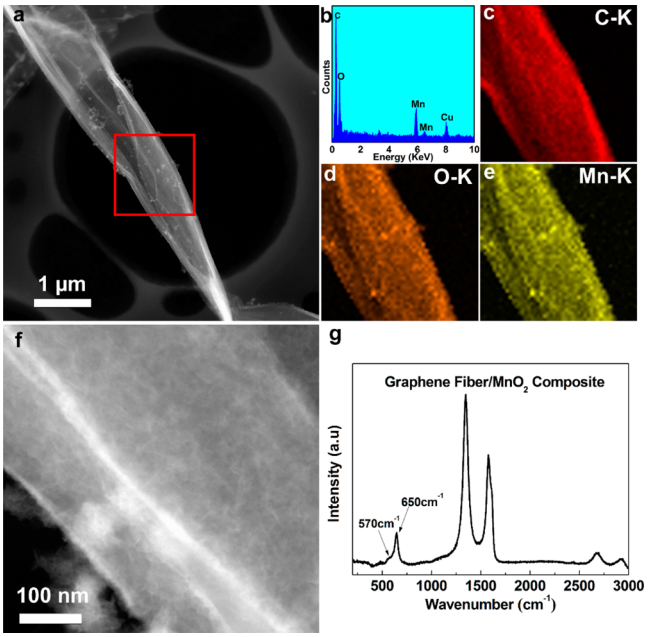

Figure 5. (a) HADDF-STEM image and (b) EDX spectrum of MnO_2/G-NF composites; (c–e) EDX mapping images of C, O, and Mn elements, respectively; and (f) corresponding high-resolution HADDF-STEM image. (g) Representative Raman spectrum of MnO_2/G-NF composites.

was further conducted, as shown in Figures 5c–e. These results clearly verify that most MnO_2 are homogeneously coated throughout the 3D fiber-like porous networks. This uniform coating of MnO_2 should be attributed to a self-limiting deposition during the redox reaction between $KMnO_4$ and the carbon on G-NFs. In addition, Raman spectroscopy and XRD patterns were further employed to check our designed MnO_2/G-NF composites as shown in Figure 5g and Figure S11 in the Supporting Information, respectively. The HR-TEM images of MnO_2 on the G-NFs (see Figure S12 in the Supporting Information) show amorphous structure which was agree well with XRD spectra. It can be seen from Figure 5g that the characteristic D and G peaks of the reduced G-NFs are located at ~1360 and 1580 cm^{-1}, respectively, and the other two peaks at 570 and 650 cm^{-1} can be assigned to the characteristic peaks of MnO_2,[44] indicating that the composite fibers contain the MnO_2 components. Furthermore, no obviously diffraction peaks from MnO_2 can be observed in XRD spectra (see Figure S11 in the Supporting Information), which indicating the coated MnO_2 layers are amorphous. This result is consistent with the previous reports which based on redox-deposited MnO_2 on carbon materials.[45]

Electrochemical performances of the flexible G-NF and MnO_2/G-NF electrodes were examined using a cyclic voltammetry (CV) method in 1 M Na_2SO_4 solution with a three-electrode system, with flexible freestanding graphene or MnO_2/Graphene film, a platinum sheet and a saturated calomel electrode (SCE) as the working, counter and reference electrodes, respectively. It is worth noting that there are no metal support or current collectors used in the tests, which can greatly reduce the mass of the electrode. As shown in Figure 6a, the CV curves of G-NS and G-NF electrodes are symmetric and rectangular, indicating an ideal electrical double layer capacitive behavior. When MnO_2 is loaded, the higher current response is observed for both MnO_2/G-NF and MnO_2/G-NS electrodes, which suggests that the introduction of MnO_2 can contribute pseudocapacitance to the total electrode. Moreover, as is expected, the current densities of G-NF and MnO_2/G-NF electrodes are almost double those of the G-NS and MnO_2/G-NS ones, respectively. In order to analyze the electrochemical performance increasing of these electrodes, BET surface area and pore size distribution were measured (as shown in Figure S13 in the Supporting Information). The adsorption–desorption isotherms of

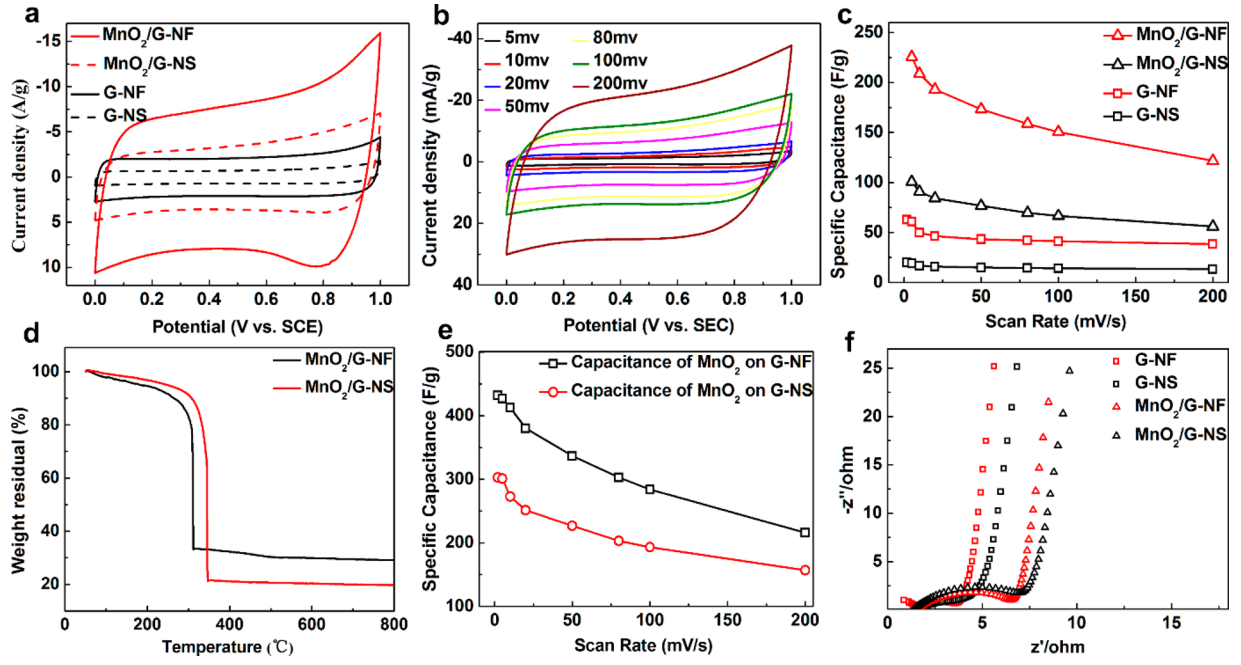

Figure 6. (a) CV curves measured at a scan rate of 10 mV/s for G-NSs, G-NFs, MnO_2/G-NSs, and MnO_2/G-NFs; (b) CV curves of MnO_2/G-NFs at various scan rates within the voltage window of 0–1 V; (c) specific capacitances of the total electrodes based on G-NSs, G-NFs, MnO_2/G-NSs, and MnO_2/G-NFs as a function of scan rate; (d) TGA curves of MnO_2/G-NSs and MnO_2/G-NFs; (e) specific capacitance of MnO_2 on G-NS- and G-NF-based electrodes as a function of scan rate; and (f) Nyquist plots of the G-NS, G-NF, MnO_2/G-NS, and MnO_2/G-NF electrodes.

G-NSs and G-NFs reveal that the BET surface area of G-NSs and G-NFs is 554 and 477 m^2/g, respectively. The specific surface area of G-NFs is a little smaller than G-NSs, which is may attribute to the curly feature of G-NFs. However, the pore size distribution of G-NFs and G-NSs shows a distinct results. Although both of the pore size mainly distributed in the range from 1 to 2 nm (micropores), the G-NFs shows higher mesopore ratio range from 2 to 50 nm. Furthermore, SEM images (as shown in Figure S2 in the Supporting Information) show that the pressed G-NFs exhibits a porous structure and G-NSs shows a relatively compact structure. The SEM images are consistent with the pore size distribution result. Thus, these differences in current densities of the MnO_2/G-NF and MnO_2/G-NS electrode can be attributed to the optimized pore structure of 3D G-NFs network, which can offer more effective pathway for effective ion migrating into the inner graphene backbone sites.

Figure 6b shows the rate-dependent CV curves from the MnO_2/G-NF electrode at scan rates from 2 to 200 mV/s within 0−1 V voltage window. It was found that CV profiles retain a relatively rectangular shape without obvious distortion with the increasing potential scan rates, demonstrating excellent high-rate performance.

Figure 6c shows the specific capacitances based on the total electrode mass of G-NSs, G-NFs, MnO_2/G-NSs, and MnO_2/G-NFs at scan rates from 2 to 200 mV/s. It can be found that the specific capacitance of the total G-NF electrode was calculated to be about 60 F/g at 2 mV/s, which is higher than that of G-NS ones (20 F/g). This increase in specific capacitance of G-NF electrode mainly attributed to their 3D porous structure, which is beneficial to the effective ion migrating into the active sites. On the other hand, the specific capacitance of the total MnO_2/G-NF electrode is as high as 225 F/g at 2 mV/s, which is more than 2 times higher than those of MnO_2/G-NS ones (102 F/g at 2 mV/s). Therefore, for nanofiber-based G-NF and G-NF/MnO_2 composite electrodes, their electrochemical performances are superior to those of nanosheet-based G-NS and MnO_2/G-NS composite electrodes, which can be attributed to their optimized porous structure.

To further make clear the main reason for the increase in specific capacitances of the two different kinds of graphene structures, the MnO_2 mass loadings were estimated using TGA. As shown in Figure 6d, the TGA curves show the MnO_2 mass loadings of 38.6 and 27.2% for G-NF and G-NS-based electrodes, respectively. These results indicate that the 3D macroporous structure of G-NF frameworks can benefit for the MnO_2 mass loadings.

Furthermore, the specific capacitive of MnO_2 on the G-NF- and G-NS-based electrodes were also investigated by cyclic voltammetry experiments at scan rates from 2 mV/s to 200 mV/s, as shown in Figure 6e. It is seen that the specific capacitance of MnO_2 on the MnO_2/G-NF electrode is as high as 432 F/g at 2 mV/s, which is approximately 1.5 times higher than that on G-NS ones (302 F/g at 2 mV/s). In addition, the specific capacitance of MnO_2/G-NF electrode gradually decreases with the scanning rates, but maintains a value as high as about 250 F/g even at 200 mV/s. Therefore, combined with the above analysis, it can be concluded that 3D graphene nanofiber network can serve as a freestanding flexible electrode as well as an ideal support for active materials.

For a deep understanding of our graphene nanofiber structure, a Nyquist plots of the G-NS, G-NF, MnO_2/GS and MnO_2/G-NF electrodes were conducted in a frequency range 0.1 Hz to 100 kHz at open-circuit voltage with an ac amplitude of 5 mV as shown in Figure 6f. The charge transfer resistances of the electrodes are calculated to be 3.2, 3.8, 5.4, and 7.2 Ω for G-NFs, G-NSs, MnO_2/G-NFs, and MnO_2/G-NSs, respectively. It was demonstrated that the nanofiber-based electrode are more beneficial to ion diffusion than that of naosheet one. In addition, the increase in the resistance is mainly attributed to the low conductivity of MnO_2. These low values of the resistances suggest a good contact between the MnO_2 and 3D graphene networks, which can also benefit a fast electron transfer.

4. CONCLUSION

In conclusion, the flexible 3D frameworks composed of winged G-NFs have been prepared by freeze-drying method assisted by MW irradiation and salt addition, followed with a scalable highly efficient chemical reduction. Furthermore, we propose an electrostatic force induced crimping mechanism for the assembly of G-NFs, where the MW irradiation can play a critical guiding role in the formation of the winged GO-NFs with edge crimped first, and the ionic strength of GO solution enhanced by salt addition will further wrinkling GO sheets into nanofibers. Benefiting from the highly porous structure and good conductive skeletons of G-NF networks, the MnO_2 loaded on G-NF frameworks exhibits a remarkably enhanced capacitance than that of G-NS ones. EC measurements indicate that the specific capacitance of MnO_2 on G-NF-based electrodes is enhanced by 43% compare to that of G-NS-based ones. Moreover, the total specific capacitance of MnO_2/G-NF electrodes is almost double that of the MnO_2/G-NS ones. This new kind of 3D structure composed of G-NFs show enhanced properties, which will make them have potential applications in the fields of high-performance catalysts, sensors, and energy storage systems.

■ ASSOCIATED CONTENT

Ⓢ Supporting Information

Calculations of the specific capacitances; additional SEM and optical images; XRD and BET results. This material is available free of charge via the Internet at http://pubs.acs.org.

■ AUTHOR INFORMATION

Corresponding Authors

*E-mail: hanwh@lzu.edu.cn.

*E-mail: xieeq@lzu.edu.cn.

Notes

The authors declare no competing financial interest.

■ ACKNOWLEDGMENTS

We acknowledge the financial support by the National Natural Science Foundation of China (61176058, 51202100, 51302122, U1232121) and the National Science Foundation for Postdoctoral Scientists of China (2012M512046)

■ REFERENCES

(1) Geim, A. K.; Novoselov, K. S. The Rise of Graphene. *Nat. Mater.* **2007**, *6*, 183−191.

(2) Das, A.; Pisana, S.; Chakraborty, B.; Piscanec, S.; Saha, S. K.; Waghmare, U. V.; Novoselov, K. S.; Krishnamurthy, H. R.; Geim, A. K.; Ferrari, A. C.; Sood, A. K. Monitoring Dopants by Raman Scattering in an Electrochemically Top-Gated Graphene Transistor. *Nat. Nanotechnol.* **2008**, *3*, 210−215.

(3) Lin, Y.-M.; Jenkins, K. A.; Valdes-Garcia, A.; Small, J. P.; Farmer, D. B.; Avouris, P. Operation of Graphene Transistors at Gigahertz Frequencies. *Nano Lett.* **2008**, *9*, 422−426.

(4) Bonaccorso, F.; Sun, Z.; Hasan, T.; Ferrari, A. C. Graphene Photonics and Optoelectronics. *Nat. Photonics* **2010**, *4*, 611−622.
(5) Nair, R. R.; Blake, P.; Grigorenko, A. N.; Novoselov, K. S.; Booth, T. J.; Stauber, T.; Peres, N. M. R.; Geim, A. K. Fine Structure Constant Defines Visual Transparency of Graphene. *Science* **2008**, *320*, 1308.
(6) Lee, C.; Wei, X.; Kysar, J. W.; Hone, J. Measurement of the Elastic Properties and Intrinsic Strength of Monolayer Graphene. *Science* **2008**, *321*, 385−388.
(7) Sun, H.; Xu, Z.; Gao, C. Multifunctional, Ultra-Flyweight, Synergistically Assembled Carbon Aerogels. *Adv. Mater.* **2013**, *25*, 2554−2560.
(8) Zangmeister, C. D.; Ma, X.; Zachariah, M. R. Restructuring of Graphene Oxide Sheets into Monodisperse Nanospheres. *Chem. Mater.* **2012**, *24*, 2554−2557.
(9) Luo, J.; Jang, H. D.; Sun, T.; Xiao, L.; He, Z.; Katsoulidis, A. P.; Kanatzidis, M. G.; Gibson, J. M.; Huang, J. Compression and Aggregation-Resistant Particles of Crumpled Soft Sheets. *ACS Nano* **2011**, *5*, 8943−8949.
(10) Xu, Z.; Sun, H.; Zhao, X.; Gao, C. Ultrastrong Fibers Assembled from Giant Graphene Oxide Sheets. *Adv. Mater.* **2013**, *25*, 188−193.
(11) Xu, Z.; Gao, C. Graphene Chiral Liquid Crystals and Macroscopic Assembled Fibres. *Nat. Commun.* **2011**, *2*, 571.
(12) Dikin, D. A.; Stankovich, S.; Zimney, E. J.; Piner, R. D.; Dommett, G. H. B.; Evmenenko, G.; Nguyen, S. T.; Ruoff, R. S. Preparation and Characterization of Graphene Oxide Paper. *Nature* **2007**, *448*, 457−460.
(13) Guo, W.; Cheng, C.; Wu, Y.; Jiang, Y.; Gao, J.; Li, D.; Jiang, L. Bio-Inspired Two-Dimensional Nanofluidic Generators Based on a Layered Graphene Hydrogel Membrane. *Adv. Mater.* **2013**, *25*, 6064−6068.
(14) He, Y.; Chen, W.; Li, X.; Zhang, Z.; Fu, J.; Zhao, C.; Xie, E. Freestanding Three-Dimensional Graphene/MnO_2 Composite Networks as Ultralight and Flexible Supercapacitor Electrodes. *ACS Nano* **2013**, *7*, 174−182.
(15) Chen, W.; He, Y.; Li, X.; Zhou, J.; Zhang, Z.; Zhao, C.; Gong, C.; Li, S.; Pan, X.; Xie, E. Facilitated Charge Transport in Ternary Interconnected Electrodes for Flexible Supercapacitors with Excellent Power Characteristics. *Nanoscale* **2013**, *5*, 11733−11741.
(16) He, Y.; Chen, W.; Zhou, J.; Li, X.; Tang, P.; Zhang, Z.; Fu, J.; Xie, E. Constructed Uninterrupted Charge-Transfer Pathways in Three-Dimensional Micro/Nanointerconnected Carbon-Based Electrodes for High Energy-Density Ultralight Flexible Supercapacitors. *ACS Appl. Mater. Interfaces* **2014**, *6*, 210−218.
(17) Li, Z.; Mi, Y.; Liu, X.; Liu, S.; Yang, S.; Wang, J. Flexible Graphene/MnO_2 Composite Papers for Supercapacitor Electrodes. *J. Mater. Chem.* **2011**, *21*, 14706−14711.
(18) He, Y.; Chen, W.; Gao, C.; Zhou, J.; Li, X.; Xie, E. An Overview of Carbon Materials for Flexible Electrochemical Capacitors. *Nanoscale* **2013**, *5*, 8799−8820.
(19) Zhou, J.; Sun, G.; Zhan, Z.; An, J.; Zhang, Y.; Zhang, Y.; Zheng, L. Polarization Behaviors of Twisted Carbon Nanotube Fibers. *J. Raman Spectrosc.* **2012**, *43*, 1221−1226.
(20) Zhou, J.; Sun, G.; Zhan, Z.; An, J.; Zheng, L.; Xie, E. Probing Structure and Strain Transfer in Dry-Spun Carbon Nanotube Fibers by Depth-Profiled Raman Spectroscopy. *Appl. Phys. Lett.* **2013**, *103*, 031912.
(21) Cong, H.-P.; Ren, X.-C.; Wang, P.; Yu, S.-H. Wet-Spinning Assembly of Continuous, Neat, and Macroscopic Graphene Fibers. *Sci. Rep.* **2012**, *2*, 613.
(22) Dong, Z.; Jiang, C.; Cheng, H.; Zhao, Y.; Shi, G.; Jiang, L.; Qu, L. Facile Fabrication of Light, Flexible and Multifunctional Graphene Fibers. *Adv. Mater.* **2012**, *24*, 1856−1861.
(23) Tian, Z.; Xu, C.; Li, J.; Zhu, G.; Shi, Z.; Lin, Y. Self-Assembled Free-Standing Graphene Oxide Fibers. *ACS Appl. Mater. Interfaces* **2013**, *5*, 1489−1493.
(24) Zeng, F.; Kuang, Y.; Wang, Y.; Huang, Z.; Fu, C.; Zhou, H. Facile Preparation of High-Quality Graphene Scrolls from Graphite Oxide by a Microexplosion Method. *Adv. Mater.* **2011**, *23*, 4929−4932.
(25) Zeng, F.; Kuang, Y.; Liu, G.; Liu, R.; Huang, Z.; Fu, C.; Zhou, H. Supercapacitors Based on High-Quality Graphene Scrolls. *Nanoscale* **2012**, *4*, 3997−4001.
(26) Wan, W.; Zhao, Z.; Hu, H.; Hao, X.; Hughes, T. C.; Ma, H.; Pan, L.; Qiu, J. Folding of Graphene into Elastic Nanobelts. *Carbon* **2014**, *76*, 46−53.
(27) Zhao, J.; Pei, S.; Ren, W.; Gao, L.; Cheng, H.-M. Efficient Preparation of Large-Area Graphene Oxide Sheets for Transparent Conductive Films. *ACS Nano* **2010**, *4*, 5245−5252.
(28) Kappe, C. O. Controlled Microwave Heating in Modern Organic Synthesis. *Angew. Chem., Int. Ed.* **2004**, *43*, 6250−6284.
(29) Schwenke, A. M.; Stumpf, S.; Hoeppener, S.; Schubert, U. S. Free-Standing Carbon Nanofibrous Films Prepared by a Fast Microwave-Assisted Synthesis Process. *Adv. Funct. Mater.* **2014**, *24*, 1602−1608.
(30) Chen, W.; Yan, L.; Bangal, P. R. Preparation of Graphene by the Rapid and Mild Thermal Reduction of Graphene Oxide Induced by Microwaves. *Carbon* **2010**, *48*, 1146−1152.
(31) Paredes, J. I.; Villar-Rodil, S.; Solís-Fernández, P.; Martínez-Alonso, A.; Tascón, J. M. D. Atomic Force and Scanning Tunneling Microscopy Imaging of Graphene Nanosheets Derived from Graphite Oxide. *Langmuir* **2009**, *25*, 5957−5968.
(32) Stankovich, S.; Dikin, D. A.; Piner, R. D.; Kohlhaas, K. A.; Kleinhammes, A.; Jia, Y.; Wu, Y.; Nguyen, S. T.; Ruoff, R. S. Synthesis of Graphene-Based Nanosheets Via Chemical Reduction of Exfoliated Graphite Oxide. *Carbon* **2007**, *45*, 1558−1565.
(33) Villar-Rodil, S.; Paredes, J. I.; Martinez-Alonso, A.; Tascon, J. M. D. Preparation of Graphene Dispersions and Graphene-Polymer Composites in Organic Media. *J. Mater. Chem.* **2009**, *19*, 3591−3593.
(34) Ferrari, A. C.; Robertson, J. Interpretation of Raman Spectra of Disordered and Amorphous Carbon. *Phys. Rev. B* **2000**, *61*, 14095−14107.
(35) Stankovich, S.; Piner, R. D.; Chen, X.; Wu, N.; Nguyen, S. T.; Ruoff, R. S. Stable Aqueous Dispersions of Graphitic Nanoplatelets Via the Reduction of Exfoliated Graphite Oxide in the Presence of Poly(Sodium 4-Styrenesulfonate). *J. Mater. Chem.* **2006**, *16*, 155−158.
(36) Zhu, Y.; Murali, S.; Stoller, M. D.; Velamakanni, A.; Piner, R. D.; Ruoff, R. S. Microwave Assisted Exfoliation and Reduction of Graphite Oxide for Ultracapacitors. *Carbon* **2010**, *48*, 2118−2122.
(37) Li, D.; Muller, M. B.; Gilje, S.; Kaner, R. B.; Wallace, G. G. Processable Aqueous Dispersions of Graphene Nanosheets. *Nat. Nanotechnol.* **2008**, *3*, 101−105.
(38) Lerf, A.; He, H.; Forster, M.; Klinowski, J. Structure of Graphite Oxide Revisited. *J. Phys. Chem. B* **1998**, *102*, 4477−4482.
(39) Cote, L. J.; Kim, F.; Huang, J. Langmuir−Blodgett Assembly of Graphite Oxide Single Layers. *J. Am. Chem. Soc.* **2008**, *131*, 1043−1049.
(40) Zangmeister, C. D. Preparation and Evaluation of Graphite Oxide Reduced at 220 °C. *Chem. Mater.* **2010**, *22*, 5625−5629.
(41) Fan, X.; Peng, W.; Li, Y.; Li, X.; Wang, S.; Zhang, G.; Zhang, F. Deoxygenation of Exfoliated Graphite Oxide under Alkaline Conditions: A Green Route to Graphene Preparation. *Adv. Mater.* **2008**, *20*, 4490−4493.
(42) Xie, W.-H.; Shiu, W.-Y.; Mackay, D. A Review of the Effect of Salts on the Solubility of Organic Compounds in Seawater. *Mar. Environ. Res.* **1997**, *44*, 429−444.
(43) Fischer, A. E.; Pettigrew, K. A.; Rolison, D. R.; Stroud, R. M.; Long, J. W. Incorporation of Homogeneous, Nanoscale MnO_2 within Ultraporous Carbon Structures Via Self-Limiting Electroless Deposition: Implications for Electrochemical Capacitors. *Nano Lett.* **2007**, *7*, 281−286.
(44) Mao, L.; Zhang, K.; On Chan, H. S.; Wu, J. Nanostructured MnO_2/Graphene Composites for Supercapacitor Electrodes: The Effect of Morphology, Crystallinity and Composition. *J. Mater. Chem.* **2012**, *22*, 1845−1851.
(45) Choi, B. G.; Yang, M.; Hong, W. H.; Choi, J. W.; Huh, Y. S. 3d Macroporous Graphene Frameworks for Supercapacitors with High Energy and Power Densities. *ACS Nano* **2012**, *6*, 4020−4028.